Insight into the Cationic Charge Distribution in $U_{1-y-z}Pu_yAm_zO_{2\pm x}$ Mixed Oxides

Pauline Fouquet-Métivier, Laetitia Medyk, Florent Lebreton, Christine Guéneau,
Myrtille O. J. Y. Hunault, Pier-Lorenzo Solari, Kathy Dardenne, Jörg Rothe, and Philippe M. Martin*

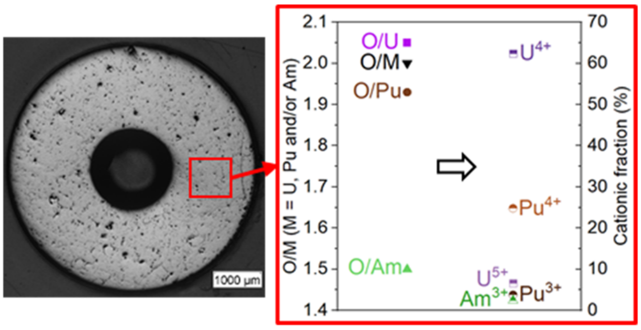

ABSTRACT: Uranium−plutonium mixed oxides, containing few mol % of Am, are currently studied as fuel for Sodium Fast Reactors. The study of the O/M ratio of these fuels is of main interest, as its variation can induce issues for reactor safety. For this purpose, four $U_{1-y-z}Pu_yAm_zO_{2\pm x}$ samples ($0.235 \leq y \leq 0.39$ and $0.005 \leq z \leq 0.02$) were studied using electron probe microanalysis (EPMA), X-ray powder diffraction (XRD), and X-ray absorption spectroscopy (XAS) experiments. EPMA analyses revealed a homogeneous matrix phase with few U- and Pu-rich agglomerates. A matrix phase of fluorite structure (face-centered cubic), as well as a small contribution of a UO_2 phase of the same structure, was evidenced for all of the samples by XRD. The O/M ratios of the $(U,Pu)O_{2\pm x}$ matrix were calculated based on the obtained lattice parameters. XANES experiments highlighted the simultaneous presence of U^{5+} and Pu^{3+}/Am^{3+} for all of the samples, indicating a charge compensation mechanism even for stoichiometric samples. Based on the EPMA and XRD results, it was evidenced that this coexistence of U^{4+}, U^{5+}, Pu^{3+}, Pu^{4+}, and Am^{3+} was not originating from the U- and Pu-rich agglomerates. It was found to be rather a peculiarity of the $U_{1-y-z}Pu_yAm_zO_{2\pm x}$ matrix phase, discussed with the help of thermodynamic calculations performed on the U−Pu−Am−O system.

INTRODUCTION

Uranium−plutonium mixed oxides (MOX) $U_{1-y}Pu_yO_{2-x}$ are considered as reference fuels for Sodium-cooled Fast Reactors (SFR). An accurate knowledge of the structural and thermodynamic properties of these fuels is mandatory to foresee their in-reactor behavior. Among them, the most important is the oxygen stoichiometry expressed as the oxygen/metal ratio (O/M ratio). Indeed, the O/M ratio of these mixed oxides conditions the behavior of the fuel in the reactor during normal and accidental conditions by influencing its thermal properties such as the thermal conductivity, melting temperature, heat capacity, and thermal expansion.[1−3] As an example, in the case of SFR, the O/M ratio has to be strictly below 2.00 but above 1.94. The lower limit is set to avoid an insufficient thermal conductivity of the oxide and thus fuel melting, whereas the upper limit is set to prevent the corrosion of the stainless steel cladding.

In stoichiometric mixed oxides (O/M = 2.00), the presence of only tetravalent cations (U^{4+} and Pu^{4+} for $U_{1-y}Pu_yO_{2.00}$) is assumed. In the hypostoichiometric domain (O/M < 2.00), the presence of oxygen vacancies is associated with a partial reduction of Pu^{4+} in Pu^{3+} (uranium remains tetravalent), while for O/M > 2.00, the introduction of oxygen interstitials leads to a partial oxidation of U^{4+} in U^{5+}/U^{6+}. Hence, the determination of the Pu^{3+}/Pu^{4+} and $U^{4+}/U^{5+}/U^{6+}$ cationic distributions allows quantification of the O/M ratio. One technique used to determine the cationic fraction in actinide and/or lanthanide mixed oxides for the quantification of the O/M ratio is the X-ray absorption spectroscopy (XAS).[4−10] Until recently, XAS results obtained at the U and Pu L_3 edges confirmed this model for uranium−plutonium mixed oxides.[6,11,12] Indeed, a recent study performed on $U_{1-y}Pu_yO_{2\pm x}$ samples cooled down after melting indicated the coexistence of U^{5+}, U^{4+}, Pu^{3+}, and Pu^{4+} for O/M < 2.00.[1] This coexistence revealed that charge compensation mechanisms occur in these mixed oxides.

An additional parameter, which could affect the O/M ratio of MOX fuels for SFR, is the plutonium isotopic composition. Indeed, due to both their targeted plutonium content ($0.20 < y < 0.40$) and the future use of plutonium originating from multirecycling of irradiated MOX fuel, an increase in the proportion of ^{241}Pu is foreseen for these fuels. The consequence of this change in the isotopic vector will be the production of ^{241}Am by β-decay of ^{241}Pu (^{241}Pu $\lambda_{1/2} = 14$ years) during the elapsed time between fabrication and irradiation, resulting in significant amount of ^{241}Am (up to 5 mol %) in the fuels. Thus, in order to accurately describe the oxygen stoichiometry of the fuel, this americium accumulation must be taken into account as its cationic charge distribution, either +III or +IV, would lead to a decrease in the O/M ratio of the fuel. Furthermore, mixed oxides containing americium such as mixed uranium−americium oxides exhibit a complex behavior, as illustrated by several publications.[5,13,14] These works showed the simultaneous presence of U^{5+} and Am^{3+} in almost equimolar proportions, leading to stoichiometric oxides of $O/(Am + U) = 2.00$, due to a charge compensation mechanism. For $Pu_{1-z}Am_zO_{2-x}$ samples, the reduction of americium from Am^{4+} to Am^{3+} was found to occur first, followed by the reduction of Pu^{4+} in Pu^{3+} once all of the americium was reduced.[10,15] Disagreements are found in the literature concerning the valence of americium in $U_{1-y-z}Pu_yAm_zO_{2\pm x}$ mixed oxides. Indeed, one study admitted that americium is purely trivalent independent of the O/M ratio,[16] while other authors assumed a mixed valence +III/+IV, depending on the oxygen stoichiometry, followed by the reduction of plutonium.[12,17−20] These results show that a proper determination of the O/M ratio in $U_{1-y-z}Pu_yAm_zO_{2\pm x}$ oxides implies an extensive knowledge of the cationic charge distribution.

Thus, as previously described, a precise knowledge of the O/M ratio of the fuel is mandatory. To this aim, additional experiments were performed in this work to determine and understand the cationic charge distribution in $U_{1-y-z}Pu_yAm_zO_{2\pm x}$. Four SFR fuels (with $0.235 \leq y \leq 0.39$ and $0.005 \leq z \leq 0.02$) were studied here using several characterization techniques, which will be described in the first part. In the second part, the determination of the chemical homogeneity and the compositions of the constituting phases will be described based on Electron Probe MicroAnalysis (EPMA) results. The crystal structures of the various fuels, studied by X-ray diffraction (XRD), and the phases, lattice parameters, as well as the O/M ratio deduced from the latter, will be presented. Finally, X-ray absorption spectroscopy (XAS) studies, in particular X-ray absorption near edge structure (XANES), performed in this work to determine the cationic charge distribution will be commented, as well as the calculated O/M ratio. The complementary results obtained with these three techniques will be used to discuss the O/M ratios obtained for these $U_{1-y-z}Pu_yAm_zO_{2\pm x}$ mixed oxides, and compared with thermodynamic calculations.

MATERIALS AND METHODS

Samples of Interest. Four batches of $U_{1-y-z}Pu_yAm_zO_{2\pm x}$ SFR fuels, with $0.235 \leq y \leq 0.39$ and $0.005 \leq z \leq 0.02$, were studied in this work. The samples were manufactured in the 1990s by comilling of UO_{2+x} and PuO_2 raw powders in various proportions to obtain the targeted plutonium content. For the four fabrications, UO_{2+x} and PuO_2 powders were cogrinded, sieved, pressed, and sintered in reducing atmosphere to obtain hypostoichiometric samples. The conditions of the sintering treatment as well as the chemical composition during manufacture are gathered in Table 1 for each batch. In this study, the samples will be referred to as MOXy with the initial Pu content (for example, MOX31).

Considering the age of the samples (manufactured between 1996 and 1999) and the initial plutonium isotopic compositions given in Table 1, variations in the initial chemical and isotopic compositions occurred. Because of the presence of ^{241}Pu in the starting PuO_2 powder, a few molar percent of ^{241}Am were produced during the storage by β-decay. Thus, prior to any measurement, the isotopic ratios, as well as the uranium, plutonium, and americium contents were quantified by thermal ionization mass spectrometry (ID-TIMS) and γ spectrometry.[21] The chemical compositions at the time of this work are given in Table 1.

Table 1. Sintering Conditions and Chemical Compositions of $U_{1-y-z}Pu_yAm_zO_{2\pm x}$ Samples of Interest during Manufacture and at the Time of This Study Determined Using Thermal Ionization Mass Spectrometry Measurements (ID-TIMS) and γ Spectrometry[21]

MOX24	1923 K, 45 min, Ar/H_2 7%	$y = 0.24$, $z = 0$, $^{238}Pu = 0.3\%$ $^{239}Pu = 69.3\%$ $^{240}Pu = 27.3\%$ $^{241}Pu = 2.1\%$ $^{242}Pu = 1.0\%$ O/M = 1.978 ± 0.002 (1999)	$y = 0.235 \pm 0.03$, $z = 0.005 \pm 0.0005$
MOX29	1923 K, 45 min, Ar/H_2 7%	$y = 0.29$, $z = 0$, $^{238}Pu = 0.3\%$ $^{239}Pu = 69.3\%$ $^{240}Pu = 27.3\%$ $^{241}Pu = 2.1\%$ $^{242}Pu = 1.0\%$ O/M = 1.973 ± 0.002 (1999)	$y = 0.28 \pm 0.03$, $z = 0.01 \pm 0.001$
MOX31	1943 K, 4 h, Ar/H_2 7%	$y = 0.31$, $z = 0$, $^{238}Pu = 2.0\%$ $^{239}Pu = 55.3\%$ $^{240}Pu = 25.4\%$ $^{241}Pu = 10.8\%$ $^{242}Pu = 6.5\%$ O/M = 1.968 ± 0.002 (1996)	$y = 0.286 \pm 0.03$, $z = 0.024 \pm 0.002$
MOX40	1923 K, 6 h, Ar/H_2 1%[22]	$y = 0.40$, $z = 0$, $^{238}Pu = 0.1\%$ $^{239}Pu = 75.4\%$ $^{240}Pu = 22.1\%$ $^{241}Pu = 1.6\%$ $^{242}Pu = 0.8\%$ O/M = 1.971 (1998)	$y = 0.39 \pm 0.03$, $z = 0.01 \pm 0.001$

EPMA. Prior to analysis, disks were cut from the pellets and put in an epoxy resin, mirror-polished, decontaminated, and metallized with carbon.

The EPMA analyses were performed at the ATALANTE facility (CEA Marcoule, France) using a CAMECA SX100 device equipped with a W source and at 20 kV. U Mα, Pu Mβ, and Am Mα peaks were observed using a PET crystal, and the O Kα peak was observed using a PC1 (W/Si) multilayer crystal. Cartographies of U, Pu, Am, and O distributions were performed, with horizontal and vertical resolutions of 1 μm, without background subtraction, with a randomly positioned scanning surface of 1 mm^2 (1024 × 1024 pixels). A current of 150 nA and a time step of 20 ms were used.

Pseudoquantitative measurements of plutonium cartographies were also obtained by comparing the plutonium content in the quantitative measurements and the number of counts in the cartographies, allowing the determination of the function between these two variables. This method was used for assessing the weight of plutonium in each pixel of the cartography, however with a high uncertainty, as the counting time is low.

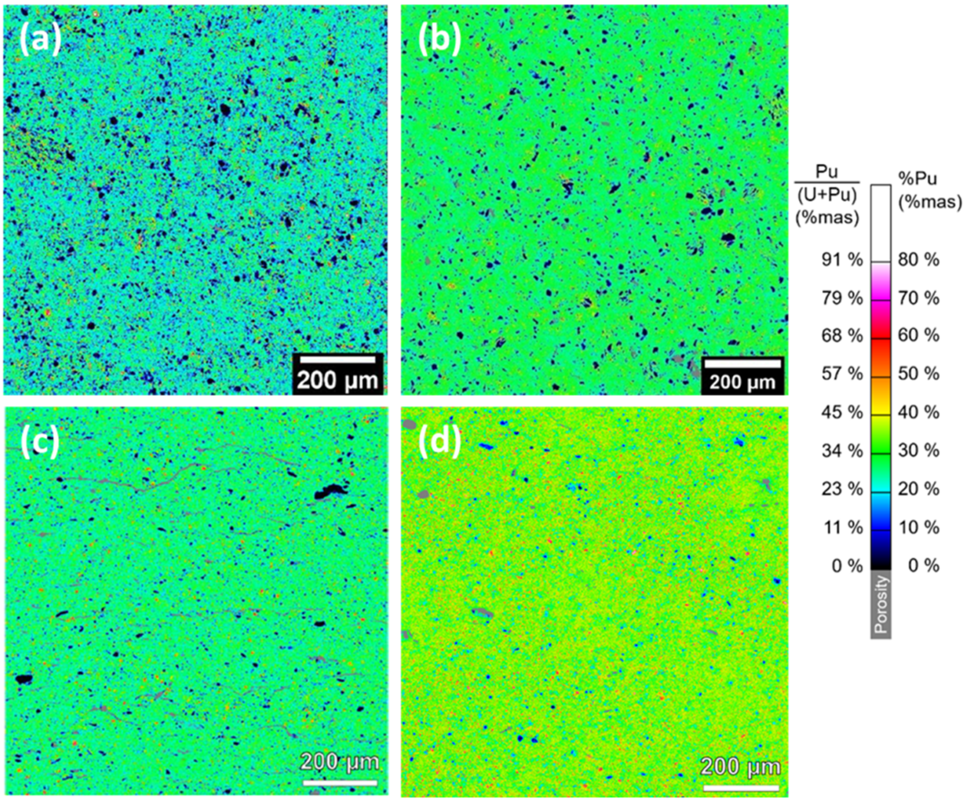

Figure 1. Cartography of the Pu distribution (false colors) determined by EPMA on a 1 mm^2 surface for (a) MOX24, (b) MOX29, (c) MOX31, and (d) MOX40. The gray spots correspond to porosities, obtained by differences in U and Pu cartographies.

XRD. XRD characterizations at ambient pressure and room temperature were performed at the ATALANTE facility at CEA Marcoule, France. The experimental setup, as well as the preparation method, was described in detail by Vauchy et al.[23] The diffractometer used presents the following characteristics: a Bruker D8 Advance diffractometer in θ–2θ Bragg–Brentano geometry, equipped with a copper source [$\lambda(K_{\alpha1}$ and $K_{\alpha2})$ = 1.5406 and 1.5444 Å] and a Bruker LYNXEYE linear detector, with a 3° 2θ opening angle. As described in ref 23, a sample stage was designed in-house and nuclearized to handle radioactive materials with no decontamination and/or decontainment of the samples. Diffraction patterns of actinide dioxides were obtained by scanning from 25 to 120° 2θ. A counting time of 0.5 s per step and step-intervals of 0.01° 2θ were chosen for most of the measurements.

Analysis and refinement of the obtained XRD patterns were performed according to the Rietveld method[24] available in the DIFFRACplus TOPAS V4 software package.[25] The peak profiles are described by a modified Thompson–Cox–Hastings pseudo-Voigt function.[26] The background is approximated by a Chebyshev polynomial function with three terms. The zero detector and background parameters were first considered during the refinement procedure, and then the lattice parameter and crystallite size were assessed. The uncertainty of the lattice parameter is estimated to be 0.001 Å.

XAS. X-ray absorption spectroscopy (XAS) analyses were performed at the MARS beamline of the SOLEIL synchrotron (Saint-Aubin, France)[27] and at the ACT station of the CAT-ACT beamline of the KIT Light Source (KARA storage ring, Karlsruhe, Germany).[28] During these experiments, both high-energy resolution fluorescence detection-X-ray absorption near edge structure (HERFD-XANES) mode and total fluorescence yield (TFY) XANES were used. The spectra were acquired at room temperature under atmospheric pressure.

Experiments Performed at the MARS Beamline (SOLEIL Synchrotron). The sample preparation was performed in a glovebox of the ATALANTE facility at the CEA Marcoule, France. Small amounts of powdered sample (1–5 mg) were mixed with boron nitride and pressed into pellets. In order to quantify the contribution of various cations of the probed elements, reference pellets were manufactured by using the same methodology applied for the samples.

HERFD-XANES and TFY-XANES analyses of the $U_{1-y-z}Pu_yAm_zO_{2\pm x}$ samples and four references were performed at the MARS beamline during two different experimental campaigns. For U^{4+} and Pu^{4+}, UO_2 and PuO_2 pellets were, respectively, chosen as reference. For Pu^{3+}, a $PuPO_4$ sample was prepared by a sol–gel route starting from PuO_2 and $(NH_4)2HPO_4$.[29] For Am^{3+}, a sample of $U_{0.90}Am_{0.10}O_{2-x}$ was used.[5] XAS spectra collected at the L_3 edge of Am at the ROBL beamline (ESRF, France) for this sample indicated that americium was present only in its trivalent state.[30]

The experiments were performed under dedicated operating conditions (2.5 GeV to 450 mA). The optics of the beamline is mainly composed of a sagittal focusing double-crystal monochromator with two sets of Si crystals and two large cylindrical mirrors, used for high-energy rejection (harmonic part) and vertical collimation/focusing, each with two different reflecting strips.

To determine the valence of uranium and plutonium, the spectra were collected at the U M_4 and Pu M_4 edges for all samples, at 3.728 and 3.970 keV, respectively. For the americium valence, the spectra were collected at the Am L_3 edge for MOX24 and MOX29 and at the Am M_5 edge for MOX31 and MOX40, at 18.51 and 3.89 keV, respectively.

For the measurements at the U and Pu M_4 edges and Am M_5 edge, the two mirrors were adjusted with the Si strips at 4 mrad and the monochromator with the Si(111) crystals. The beam spot size was 300 μm × 150 μm at full width at half-maximum (H × V). The incident energy was calibrated using the absorption K-edge of potassium in KBr (3.608 keV). The HERFD-XANES spectra were obtained using a Johann-type X-ray emission spectrometer with Rowland circle focusing geometry using a spherically bent Si(220) crystal with 1 m bending radius coupled to a fluorescence single-element KETEK silicon drift detector. The M_β emission lines of U

(3.337 keV) and Pu (3.533 keV) and the $M_{\alpha1}$ emission line of Am (3.445 keV) were selected. The samples were oriented at 45° to the incident beam. A He-filled chamber was located between the samples, the crystal, and the detector in order to reduce the scattering and absorption by air of the emitted and incident X-ray. Based on the full width at half-maximum of the peak of elastic diffraction located at the double energy, the global energetic resolution of the emission spectrometer was determined to be equal to 0.5 eV in the range of 3.3−3.5 keV.

For the measurements at the Am L_3 edge, the two mirrors were adjusted with Pt strips at 2.7 or 3.1 mrad and the monochromator with the Si(220) crystals. The TFY-XANES signals were measured using a four-element HITACHI silicon drift detector. The energy calibration was performed using a Zr foil (K-edge at 17.998 keV).

Experiment Performed at the CAT-ACT Beamline (KARA Synchrotron). Only one reference, AmO_2 for Am^{4+}, was analyzed by HERFD-XANES at the ACT beamline (M_5 edge at 3.89 keV). A Si(111) double-crystal monochromator was used with vertically collimating and toroidally focusing Si mirrors. The beam spot size was reduced to 500 x 500 μm by slits in front of the sample. The HERFD-XANES spectra were obtained also in this case using a Johann-type X-ray emission spectrometer with Rowland circle focusing geometry including four spherically bent Si(220) crystals with 1 m bending radius and a single-element KETEK silicon drift detector. The X-ray emission spectrometer and the sample were placed inside a glovebox, maintaining a constant He flow so that less than 0.1% O_2 was present in the box during the measurements. This was necessary to minimize the intensity loss due to scattering and absorption of the 3−4 keV X-ray photons in air. The $M\alpha_1$ emission line of Am (3.445 keV) was selected. The uncertainty on the energy positions of the spectra was estimated as ±0.05 eV.

Data Analysis. The HERFD-XANES spectra at the M_4 and M_5 edges were normalized at the maximum of absorption using the Athena software, while the spectra at the L_3 edge were normalized with pre- and postedge linear functions.[31] The normalized spectra were refined by a linear combination of the reference spectra in order to quantify the contribution of various probed cations. Spectra at the U M_4 edges of U_4O_9 and U_3O_8 previously collected on the ID26 beamline of the ESRF (Grenoble, France) were used as reference for U^{5+} and U^{6+}[32,33], while the spectra of UO_2 collected at the MARS beamline were used for U^{4+}. Spectra collected at the Pu M_4 edge of PuO_2 and $PuPO_4$ at the MARS beamline were used as reference for Pu^{4+} and Pu^{3+}, respectively. For the Am M_5 edge, spectra collected at the MARS beamline for $U_{0.90}Am_{0.10}O_{2-x}$ (Am^{3+}) and at the ACT beamline for AmO_2 (Am^{4+}) were used. For the Am L_3 edge, spectra of AmO_2 and $U_{0.90}Am_{0.10}O_{2-x}$ previously collected at the ROBL beamline of the ESRF were used as reference for Am^{4+} and Am^{3+}.[30]

RESULTS

Chemical Composition. Examples of pseudoquantitative cartography in the Pu content are given in Figure 1 for the four samples, where similar results were obtained visually, with a homogeneous distribution of Pu within the $U_{1-y-z}Pu_yAm_zO_{2\pm x}$ matrix. However, some uranium-rich and plutonium-rich agglomerates are observed in dark blue and red, respectively. The uranium-rich zones exhibit a composition close to the one of UO_2, whereas the ones of plutonium have a maximum Pu content of 60 wt %. The sizes of these clusters are around a few tens of micrometers and around a few micrometers for uranium-rich and plutonium-rich zones, respectively.

As an example, the surface distribution of the Pu content obtained for the MOX29 sample is plotted in Figure 2. For the four samples, a monomodal distribution, refined using a Gaussian function, is observed for the $U_{1-y-z}Pu_yAm_zO_{2\pm x}$ matrix composition. The position of the main mode indicates the average plutonium content of the matrix phase. A shoulder is observed for $0 < y < 0.17$, indicating the presence of uranium-rich agglomerates. By calculating the area under the curve for this range, it was possible to quantify the surface fraction of these agglomerates, equal to 8 surf % for the U-rich cluster in the case of the MOX29 sample. A small proportion (around 5 surf %) of Pu-rich agglomerates is also visible with a higher plutonium content, with y ranging between 0.40 and 0.50. For MOX40, fewer uranium-rich or plutonium-rich agglomerates are evidenced while fitting the plutonium content distribution, resulting in proportions of agglomerates lower than 2 surf %.

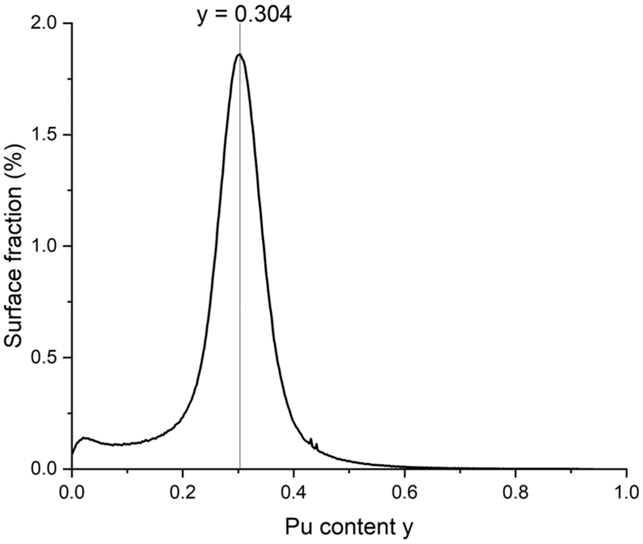

Figure 2. Gaussian surface distribution of the Pu content within the scanned areas of the MOX29 sample.

The average Pu contents obtained using the Gaussian distribution and the surface proportions of U- and Pu-rich agglomerates are summarized in Table 2 for the four samples.

Table 2. Pu Content of the $U_{1-y-z}Pu_yAm_zO_{2\pm x}$ Matrix Phase and Proportions of U- and Pu-Rich Agglomerates Obtained by EPMA for MOX24, MOX29, MOX31, and MOX40

sample	Pu/(U+Pu) content of the matrix (wt %)	U-rich agglomerates (surf %)	Pu-rich agglomerates (surf %)
MOX24	24.3 ± 0.5%	10%	4%
MOX29	30.4 ± 0.4%	8%	5%
MOX31	28.6 ± 0.5%	5%	3%
MOX40	38.2 ± 0.3%	3%	2%

It can be noticed that the Pu content determined by EPMA analyses slightly differs from the one measured by chemical analyses (Table 1). Indeed, in the EPMA analyses, the value obtained corresponds to the composition of the matrix phase, whereas the value expressed in Table 1 refers to the whole sample, taking also into account the U-rich and Pu-rich zones.

Crystal Structure. Two face-centered cubic structures (fcc) or fluorite-type phases were systematically observed for all of the samples. The diffraction pattern obtained for MOX29 is presented in Figure 3 as an example. The lattice parameters and proportions of the two phases obtained by Rietveld refinement are summarized in Table 3. Based on the EPMA results described in section Chemical Composition, the main phase was attributed to the $U_{1-y-z}Pu_yAm_zO_{2\pm x}$ matrix and the other phase was attributed to UO_2 for all of the samples. It can

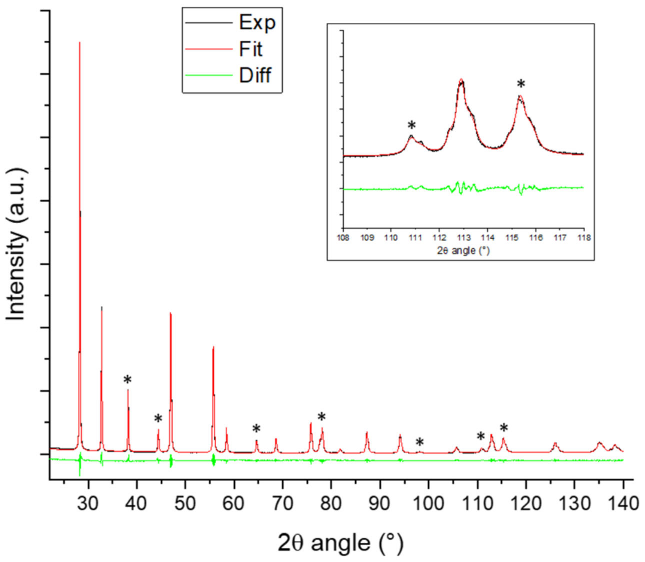

Figure 3. XRD pattern of a MOX29 sample (*: XRD reflections of the internal Au standard).

be noticed that the lattice parameter reported for the UO_2 phase (a = 5.482 ± 0.001 Å) differs from the one recommended (5.470 Å). Oxidation of UO_2 into hyperstoichiometric UO_{2+x} was excluded as it would lead to a decrease in the lattice parameter. Thus, the difference observed here can possibly be explained by a swelling of UO_2 lattice due to the accumulation of He, generated by Pu α-decay present in the surrounding $U_{1-y-z}Pu_yAm_zO_{2\pm x}$ matrix.[34]

In the case of the MOX40 sample, as no significant proportion of U-rich agglomerates was observed by EPMA (Table 2), the attribution of this second phase to a UO_2 phase can be questioned. The first reason is the small percentage of second phase determined by Rietveld analyses (<5%). The second is the value of the lattice parameter, similar to that of the UO_2 phases of the MOX29 and MOX31 samples. Moreover, based on the EPMA map and Pu content distribution, no broad distribution or second matrix phase is evidenced.

Because of the aging of the samples, swelling of the lattice with time, induced by α-decay, occurred in the materials. This phenomenon was taken into account when correcting the obtained lattice parameters using the formula of Kato et al.,[35] knowing the initial isotopic composition and the storage time of the samples (available in Table 1). For all samples, based on the elapsed time between the manufacturing and the study (between 25 and 30 years), the swelling of the lattice reached the saturation value, corresponding to an increase of 0.29% of the initial cell parameter. Using the corrected lattice parameter, the O/M ratio was then determined using the relation of Duriez et al., linking the fluorite cell parameter, the plutonium content, and the deviation from stoichiometry.[36] The plutonium content determined by EPMA for the matrix phase was used. The results obtained for all of the phases are given in Table 3. By combination of the proportions of the phases and the corresponding O/M ratio, the global O/M ratio of the samples was determined (see Table 3).

Cationic Charge Distribution. XANES spectra collected at the U M_4, Pu M_4, Am M_5, and Am L_3 edges are represented in Figure 4 for the samples and the different reference compounds.

When looking at the U M_4 edge, the white line positions (maxima of the spectra) of the four MOX samples correspond to the one of UO_2. No contribution of U_3O_8 is noticed, thus no U^{6+} is present in the samples. Moreover, the shoulder observed around 3723.8 eV, corresponding to the second maximum of U_4O_9, attributed to U^{5+}, evidences the presence of pentavalent uranium in the samples. A mixed valence U^{4+}/U^{5+} is thus systed, the resulting O/U ratios obtained with the respective proportions of the cations are all hyperstoichiometric (O/U > 2.00).

For the Pu M_4 edge, a shoulder is observed around 3966.2 eV, indicating the contribution of trivalent Pu, also highlighted by the diminution in the intensity of the peak located at 3970 eV, compared to the one of PuO_2. A reduction of plutonium, with a mixed valence of Pu^{3+}/Pu^{4+}, is systematically observed, and thus, the O/Pu ratios are all lower than 2.00.

Finally, for the Am M_5 edge, considering the signal/noise ratio, the white line positions of the two samples are considered equal to the one of the Am^{3+} cation. The same observation is made at the Am L_3 edge, where the white line positions overlap the one of $U_{0.90}Am_{0.10}O_{2-x}$. Thus, for all of the samples studied here, the O/Am ratio is equal to 1.50.

The proportions of the various cations were determined by a linear combination of the reference spectra and are given in Table 4, as well as the O/M ratio with M = U, Pu, and Am, obtained for the four samples.

By combining the results of O/U, O/Pu, and O/Am in Table 4 and the Pu content determined by EPMA, the following O/M ratios are obtained: 1.98 ± 0.01 for MOX24 and MOX29 and 2.00 ± 0.01 for MOX31 and MOX40 (Table 5). These data correspond to a global O/M ratio at the scale of

Table 3. Refined Lattice Parameters and Estimated O/M Ratio of $U_{1-y-z}Pu_yAm_zO_{2\pm x}$ Samples

samples	phases	proportion	raw lattice parameter (±0.001) (Å)	corrected lattice parameter (Kato et al.[35]) (±0.001) (Å)	O/M ratio (±0.005)	global O/M ratio (±0.005)
MOX24	Matrix $U_{1-y-z}Pu_yAm_zO_{2\pm x}$	>95%	5.473	5.457	1.984	1.985
	UO_2	<5%	5.483		2.000	
MOX29	Matrix $U_{1-y-z}Pu_yAm_zO_{2\pm x}$	92%	5.469	5.453	1.982	1.984
	UO_2	8%	5.482		2.000	
MOX31	Matrix $U_{1-y-z}Pu_yAm_zO_{2\pm x}$	95%	5.463	5.447	2.005	2.004
	UO_2	5%	5.475		2.000	
MOX40	Matrix $U_{1-y-z}Pu_yAm_zO_{2\pm x}$	>95%	5.459	5.443	1.995	1.995
	UO_2	<5%	5.482		2.000	

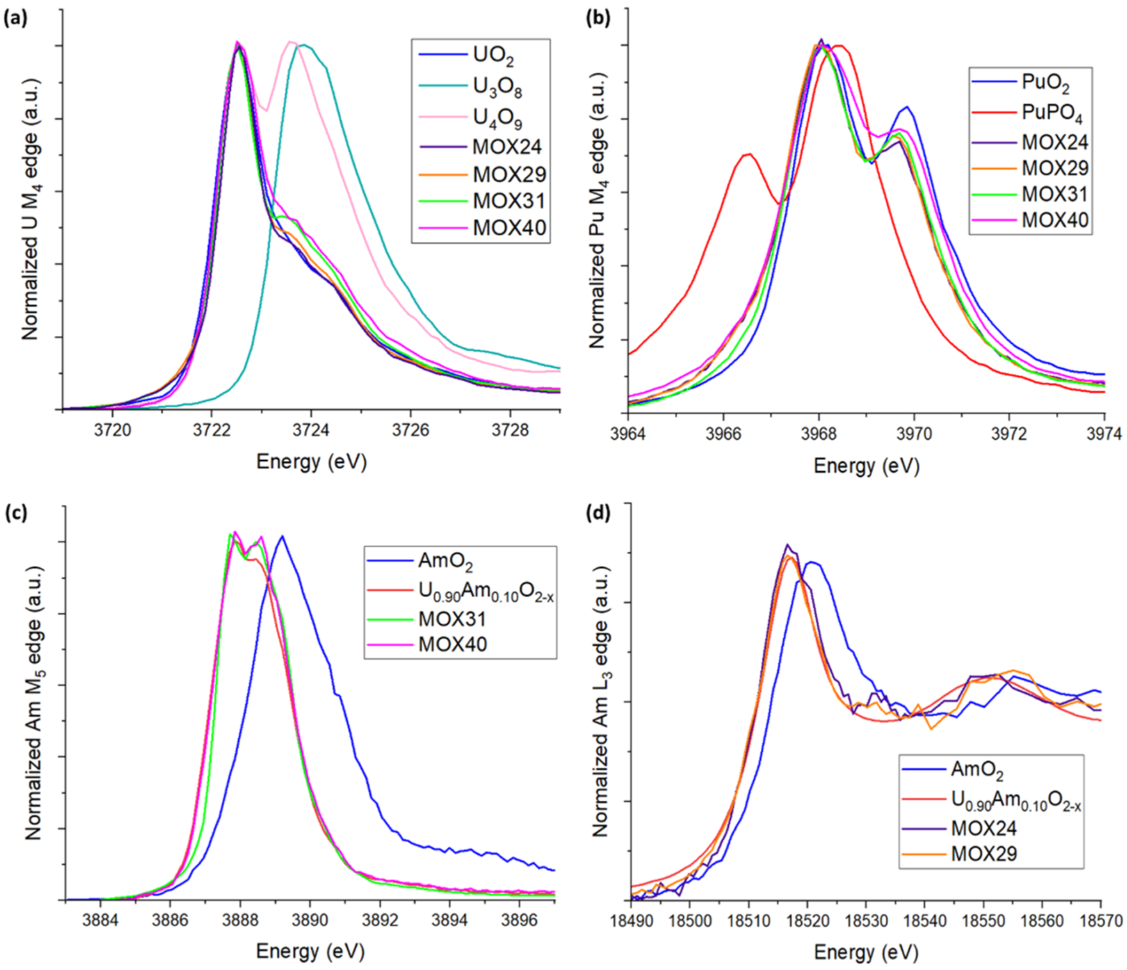

Figure 4. XANES spectra collected at (a) U M_4, (b) Pu M_4, (c) Am M_5, and (d) Am L_3 edges for the MOX24, MOX29, MOX31, and MOX40 samples and their references.

Table 4. Proportions of Cations of the Probed Elements Obtained Experimentally by XANES

	U M_4 edge			Pu M_4 edge		Am M_5 edge	
sample	U^{4+} (%)	U^{5+} (%)	U^{6+} (%)	Pu^{4+} (%)	Pu^{3+} (%)	Am^{4+} (%)	Am^{3+} (%)
MOX24	96.7 ± 1.0	3.3 ± 1.0	0	76.8 ± 1.0	23.2 ± 1.0	0 ± 0.3	100 ± 0.3
MOX29	94.9 ± 1.0	5.10 ± 1.0	0	74.7 ± 2.0	25.3 ± 2.0	0 ± 0.3	100 ± 0.3
MOX31	90.5 ± 1.2	9.50 ± 1.2	0	86.7 ± 1.8	13.3 ± 1.8	0 ± 0.3	100 ± 0.3
MOX40	89.7 ± 0.6	10.3 ± 0.6	0	90.1 ± 0.8	9.90 ± 0.8	0 ± 0.3	100 ± 0.3

Table 5. O/M Ratios (M = U, Pu, Am, and U + Pu + Am) Determined by XANES, Calculated Using the Pu Content Determined by EPMA, Compared to the Ones Determined by XRD

sample	O/U	O/Pu	O/Am	O/M ratio determined by XANES (±0.01)	O/M ratio determined by XRD (±0.005)
MOX24	2.02	1.89	1.50	1.98	1.985
MOX29	2.03	1.87	1.50	1.98	1.984
MOX31	2.05	1.93	1.50	2.00	2.004
MOX40	2.05	1.95	1.50	2.00	1.995

the pellet, taking also into account the heterogeneities and uranium-rich and plutonium-rich agglomerates evidenced by EPMA. A good agreement is found with the O/M ratios determined using the lattice parameters obtained by X-ray diffraction, reported in Table 5.

DISCUSSION

As evidenced in Table 4, small proportions of U^{5+} and Pu^{3+} systemically coexist in the materials, even for stoichiometric samples such as MOX31 or MOX40. The coexistence of U^{4+}, U^{5+}, Pu^{4+}, and Pu^{3+} was already observed in ref 1, for $U_{1-y}Pu_yO_{2\pm x}$ samples, molten under air or Ar. In addition, americium purely in its trivalent state is also observed in this work. Prieur et al. already observed this phenomenon for $U_{1-z}Am_zO_{2-x}$ samples of similar fluorite structure, with the simultaneous presence of U^{4+}, U^{5+}, and Am^{3+}.[13,37] These observations imply that an O/M ratio of 2.00 does not necessarily correspond to ions only in their tetravalent state.

It appears that a charge compensation mechanism occurs here, as already discussed by Osaka et al.[16,18] Indeed, as the oxygen potential of AmO_{2-x} is high, tetravalent americium is unstable and americium will be present only in its trivalent oxidation state.[38] Thus, Osaka et al. expect that once all of the americium is reduced to Am^{3+}, plutonium will start to be reduced as well.[16,18] For a mixed oxide of the formula $U_{1-y-z}Pu_yAm_zO_{2-x}$, two domains are evidenced by their model: $O/M < 2 - \frac{z}{2}$ and $O/M > 2 - \frac{z}{2}$. For the first region, americium is supposed to be trivalent, while uranium is expected to remain tetravalent. On the contrary, for the second region, the interactions between uranium and americium are predominant, resulting in trivalent americium and pentavalent uranium to maintain the electrical neutrality.[16,18] The regions of the model and the corresponding cations expected in this work are compared to the cations observed experimentally in Table 6. A disagreement between the model and the results of MOX24 and MOX29 samples is noticed here for the uranium cations. Indeed, in this work, U^{5+} is observed in the four samples, while it should not be present for MOX24 and MOX29. For the plutonium cations, a disagreement is observed for MOX31 and MOX40 samples. Indeed, a partial reduction of Am in Am^{3+} is stated by Osaka et al., contrary to the fact that in this work, all of the americium present in the sample is reduced. For these two samples, trivalent plutonium is also observed.

Table 6. Comparison between the Cations Expected by the Model of Osaka et al.[16,18] and the Ones Determined Experimentally (Underlined in Bold Is the Disagreement between the Model of Osaka and This Work)

sample	$2 - z/2$	domain	expected cations according to Osaka et al.[16,18]	cations observed experimentally in this work
MOX24 (O/M = 1.98 ± 0.01, $z = 0.005$)	1.998	$O/M < 2 - \frac{z}{2}$	U^{4+} Pu^{4+} Pu^{3+} Am^{3+}	$\underline{\mathbf{U^{5+}}}$ U^{4+} Pu^{4+} Pu^{3+} Am^{3+}
MOX29 (O/M = 1.98 ± 0.01, $z = 0.01$)	1.995	$O/M < 2 - \frac{z}{2}$	U^{4+} Pu^{4+} Pu^{3+} Am^{3+}	$\underline{\mathbf{U^{5+}}}$ U^{4+} Pu^{4+} Pu^{3+} Am^{3+}
MOX31 (O/M = 2.00 ± 0.01, $z = 0.02$)	1.99	$O/M > 2 - \frac{z}{2}$	U^{5+} U^{4+} Pu^{4+} Am^{3+}	U^{5+} U^{4+} Pu^{4+} $\underline{\mathbf{Pu^{3+}}}$ Am^{3+}
MOX40 (O/M = 2.00 ± 0.01, $z = 0.01$)	1.995	$O/M > 2 - \frac{z}{2}$	U^{5+} U^{4+} Pu^{4+} Am^{3+}	U^{5+} U^{4+} Pu^{4+} $\underline{\mathbf{Pu^{3+}}}$ Am^{3+}

In order to try to explain the simultaneous presence of U^{5+} and Pu^{3+}/Am^{3+}, the EPMA and XRD results were investigated. The example of the MOX40 sample will be taken here, but the same explanation is valid for the other samples.

The proportions of U- and Pu-rich agglomerates, given in Table 2, are respectively 3 and 2 surf %, resulting in a matrix phase representing 95% of the scanned surface of the sample. The porosity was excluded from this analysis.

Considering first the case of plutonium, with a Pu content of 38.2%, plutonium represents 36.3% of the surface of the matrix phase. The same calculation is performed for the Pu-rich agglomerates, for which the Pu content is assumed to be approximately 70.0%, resulting in 1.4% of the surface of the agglomerates. At the scale of the scanned surface, summing the plutonium of the matrix and of the agglomerates leads to a total surface proportion of 37.7%. Thus, the agglomerates represent 3.7% of the whole plutonium for the MOX40 sample. Assuming that the plutonium in the agglomerates would be purely trivalent (the most extreme hypothesis leading to an unrealistic Pu_2O_3 composition), and knowing that the matrix phase is stoichiometric (see Table 3) and does not contain any Pu^{3+} ions as stated in the model of Osaka et al., the maximum amount of Pu^{3+} present in the sample would be 3.7%. This result is not in agreement with the proportion of Pu^{3+} determined experimentally (9.90 ± 0.8%) given in Table 4.

The same reasoning can be applied to uranium. Assuming that the uranium in the U-rich agglomerates (assumed to contain 90% of U) would be purely pentavalent, corresponding to a highly hypothetical U_2O_5 composition, the total amount of U^{5+} in the sample would be 4.4%. However, according to Table 4, pentavalent uranium represents 10.3% of the total uranium. The XRD results previously obtained also invalidate the presence of U^{5+} in the U-rich agglomerates. Indeed, assuming that the second phase of U-rich agglomerates is UO_{2+x}, a decrease in the lattice parameter of the UO_2 phase, linked to oxidation, would be observed. However, this statement is not supported by the lattice parameters previously determined, as an increase is noticed.

In conclusion, the simultaneous existence of U^{5+} and Pu^{3+}/Am^{3+} does not originate from the U- and Pu-rich agglomerates and is thus linked to the matrix phase. This peculiarity of $U^{4+}/U^{5+}/Pu^{3+}/Pu^{4+}/Am^{3+}$ multivalence has been observed here for the first time in $(U,Pu)O_{2\pm x}$ mixed oxides, contrary to previous studies.[7,11,12] This could be thanks to the technique used in this study, the HERFD-XANES, which has the specificity of being more sensitive than the classic XANES technique.[8]

In order to try to understand the origins of this multivalence, the experimental results obtained in this work were compared to the cationic distribution obtained using thermodynamic modeling of the U−Pu−Am−O system. In this case, the CALPHAD method was used[39] and the calculations were performed with the Thermo-Calc software (version 2024a).[40] The following models were used in this work: Kurata for U−Pu,[41] Guéneau et al. for U−O,[42] Epifano et al. for Am−O,[43] Guéneau et al. modified for the liquid by Fouquet-Métivier et al. for Pu−O and U−Pu−O,[1,42] Epifano for U−Am−O,[44,45] and Fouquet-Métivier for Pu−Am−O.[46] In this model, the $U_{1-y-z}Pu_yAm_zO_{2\pm x}$ mixed oxide is described using a three-sublattice model as follows: $(U^{3+}, U^{4+}, U^{5+}, Pu^{3+}, Pu^{4+}, Am^{3+}, Am^{4+})(O^{2-}, Va)_2(O^{2-}, Va)$. The first sublattice corresponds to the cationic site, the second to the normal site for oxygen in the fluorite structure, where the addition of vacancies "Va" allows describing the hypostoichiometry, and the third sublattice to the site for interstitial oxygen, corresponding to the hyperstoichiometric composition range.

From this model, the cationic site fractions of the cationic species in the $U_{1-y-z}Pu_yAm_zO_{2\pm x}$ phase were calculated at 1923 K, the sintering temperature at which the O/M ratio is assumed to be fixed. The results calculated for the compositions of the four MOX samples are given in Table 7 and compared with the ones obtained experimentally in Table 4.

For the uranium cations, a small contribution of U^{3+} is systematically predicted for all of the samples, originating from the U−O model, whereas it has not been found experimentally. The proportions of U^{4+} and U^{5+} calculated for the MOX24 sample are in good agreement with those obtained experimentally. A small disagreement is found for MOX29 and MOX31, with an underestimation of the proportion of U^{5+} of 1.8% for MOX29 and 2.1% for MOX31. This disagreement then increases for MOX40, with an underestimation of 5.7%.

For the plutonium cations, a systematic underestimation of the proportion of Pu^{3+} is calculated for all of the samples, with 4.1% difference for MOX24, 10.3% for MOX29, 7% for

Table 7. Thermodynamic Calculations of the Cationic Distributions for the $U_{1-y-z}Pu_yAm_zO_{2\pm x}$ Phase at 1923 K for the Compositions of the Four MOX Samples

	U^{3+} (%)	U^{4+} (%)	U^{5+} (%)	Pu^{3+} (%)	Pu^{4+} (%)	Am^{3+} (%)	Am^{4+} (%)
$y = 0.235$, $z = 0.005$, O/M = 1.985 (MOX24)	0.2	96.8	3	19.1	80.9	100	0
$y = 0.28$, $z = 0.01$, O/M = 1.984 (MOX29)	0.2	96.6	3.2	15.0	85.0	100	0
$y = 0.286$, $z = 0.024$, O/M = 2.004 (MOX31)	0.2	92.5	7.3	6.3	93.7	100	0
$y = 0.39$, $z = 0.01$, O/M = 1.995 (MOX40)	0.3	95.0	4.7	6.7	93.3	100	0

MOX31, and 3.2% for MOX40. The effect of a decrease of the oxygen stoichiometry could explain the difference in the results, as it would increase the Pu^{3+} content. However, no clear trend is evidenced.

Last, it can be noted that the cationic proportions of americium are in agreement with the experimental findings, with 100% trivalent americium.

This work demonstrates that, contrary to what is being commonly accepted, an oxygen/metal ratio equal to 2.00 for $U_{1-y-z}Pu_yAm_zO_{2.00}$ mixed oxides is not correlated to only tetravalent cations, as already observed by Epifano et al. for $U_{1-z}Am_zO_{2.00}$ samples[5] and contrary to what has been used in the past for $U_{1-y}Pu_yO_{2.00}$ samples.[16,18,47] This multivalence evidenced experimentally can be explained by looking at the subsystems of the U−Pu−Am−O system through thermodynamic calculations and defect chemistry. Indeed, when looking at the U−O system,[42,48] in stoichiometric $UO_{2.00}$, polarons are forming at a high temperature, with small contributions of U^{3+} and U^{5+} in the same proportions, as well as Frenkel pairs of oxygen with the same proportions of oxygen vacancies and interstitial oxygen. At a high temperature, when adding Pu to UO_2, as PuO_{2-x} exhibits a higher oxygen potential than $UO_{2\pm x}$,[49] Pu^{4+} will be the first cation to be reduced into Pu^{3+}. Thus, the following cations will be present in $U_{1-y}Pu_yO_{2-x}$: U^{3+}, U^{4+}, U^{5+}, Pu^{3+}, and Pu^{4+}. Then, when adding Am to the system, the same reasoning is applied, as $\Delta G_{O_2}(AmO_{2-x}) > \Delta G_{O_2}(PuO_{2-x}) > \Delta G_{O_2}(UO_{2\pm x})$.[49] Thus, americium is systematically present as Am^{3+}, and as the latter is more stable than Pu^{3+}, a decrease in the proportion of Pu^{3+} in the system will be observed. Based on these observations, the simultaneous presence of U^{5+}, Pu^{3+}, and Am^{3+} can be explained in $U_{1-y-z}Pu_yAm_zO_{2\pm x}$. Therefore, all of these cations and the interactions between them need to be taken into account to better describe these oxides.

CONCLUSIONS

The chemical compositions and structures of four $U_{1-y-z}Pu_yAm_zO_{2\pm x}$ samples (with $0.235 \leq y \leq 0.39$ and $0.005 \leq z \leq 0.02$) were investigated in this work. The plutonium distribution was found to be homogeneous by EPMA, however, with few uranium-rich and plutonium-rich agglomerates. A monomodal distribution was obtained for the Pu distribution within the matrix phase, allowing the determination of the proportions and Pu contents for the agglomerates. When collecting XRD patterns at room temperature, two phases were observed: one matrix $U_{1-y-z}Pu_yAm_zO_{2\pm x}$ phase and one UO_2 phase, in agreement with the agglomerates observed by EPMA. The lattice parameters determined in this work were corrected to take into account the self-irradiation of the samples and used to calculate the O/M ratio. Finally, the cationic charge distribution determined by XANES evidenced the presence of a mixture of cations, with simultaneously U^{4+}, U^{5+}, Pu^{4+}, Pu^{3+}, and Am^{3+}. The O/M ratios were found to be in agreement with the ones determined by XRD. The simultaneous presence of U^{5+} and Pu^{3+}/Am^{3+} highlighted a charge compensation mechanism. Thanks to the results obtained by EPMA and XRD, it was determined that this presence of both pentavalent and trivalent cations in stoichiometric mixed oxides was not caused by the presence of U-rich and Pu-rich agglomerates but originated from a peculiarity of the $U_{1-y-z}Pu_yAm_zO_{2\pm x}$ matrix phase. In addition, the simultaneous multivalence of U^{4+}, U^{5+}, Pu^{4+}, Pu^{3+}, and Am^{3+} was explained in this work with the help of thermodynamic calculations using the CALPHAD method, coming back to the subsystems of the U−Pu−Am−O system.

Further investigations are mandatory to understand this phenomenon. In particular, performing in situ characterizations such as XANES would allow us to determine if this is a constant phenomenon throughout the temperature range between the one of the sintering and room temperature or if it occurs at a precise temperature. In addition, a preliminary hypothesis would be that this duality could be linked to α self-irradiation, as it has not been observed in previous studies on just-sintered $U_{1-y}Pu_yO_{2\pm x}$ oxides. In particular, the presence of point defects or extended defects such as dislocations could influence oxygen diffusion within the material.[50,51] In order to study the influence of the defects on oxygen diffusion, transmission electron microscopy (TEM) studies would be of interest.

AUTHOR INFORMATION

Corresponding Author

Philippe M. Martin − *CEA, DES, ISEC, DMRC, Université Montpellier, Marcoule, 30207 Bagnols-sur-Cèze, France*; Email: philippe-m.martin@cea.fr

Authors

Pauline Fouquet-Métivier − *CEA, DES, ISEC, DMRC, Université Montpellier, Marcoule, 30207 Bagnols-sur-Cèze, France*; Present Address: CEA, DES, IRESNE, DEC, Cadarache F-13108 Saint-Paul-Lez-Durance, France; orcid.org/0000-0002-9513-1796

Laetitia Medyk − *CEA, DES, ISEC, DMRC, Université Montpellier, Marcoule, 30207 Bagnols-sur-Cèze, France*

Florent Lebreton − *CEA, DES, ISEC, DMRC, Université Montpellier, Marcoule, 30207 Bagnols-sur-Cèze, France*; orcid.org/0000-0003-4714-8021

Christine Guéneau − *Université Paris-Saclay, CEA, Service de recherche en Corrosion et Comportement des Matériaux, 91191 Gif-sur-Yvette, France*

Myrtille O. J. Y. Hunault − *MARS beamline, Synchrotron SOLEIL, 91190 Saint-Aubin, France*; orcid.org/0000-0002-3754-8630

Pier-Lorenzo Solari − *MARS beamline, Synchrotron SOLEIL, 91190 Saint-Aubin, France*

Kathy Dardenne − *Institute for Nuclear Waste Disposal (INE), Karlsruhe Institute of Technology, 76344 Eggenstein-Leopoldshafen, Germany*

Jörg Rothe − *Institute for Nuclear Waste Disposal (INE), Karlsruhe Institute of Technology, 76344 Eggenstein-Leopoldshafen, Germany;* orcid.org/0000-0001-5366-2129

Author Contributions

The manuscript was written through contributions of all authors. All authors have given approval to the final version of the manuscript.

Notes

The authors declare no competing financial interest.

ACKNOWLEDGMENTS

This work was supported by the cross-cutting basic research Program (RTA Program) of the CEA Energy Division. The authors thank the ESFR-SMART Project (funded by the Euratom Research and Training Programme 2014−2018 under Grant Agreement No. 754501) for providing the (U, Pu, Am)$O_{2\pm x}$ samples. O. Walter, K. Popa, and D. Robba, the JRC-Karlsruhe technical staff as well as the ATALANTE technical staff (CEA Marcoule), are acknowledged for their help in the sample preparation for the XANES measurements. The authors thank the SOLEIL synchrotron for providing the synchrotron beam facilities, as well as the radioprotection unit, for the experiments performed on the MARS beamline (Projects 20192011 and 20210255). The authors acknowledge the KIT Light Source for provision of beamtime at the CAT-ACT beamline and thank the Institute for Beam Physics and Technology (IBPT) for the operation of the storage ring, providing the beam in the Karlsruhe Research Acceleration (KARA). This research contributes to the SESAM pilot project of the Joint Program on Nuclear Materials (JPNM) of the European Energy Research Alliance (EERA).

REFERENCES

(1) Fouquet-Métivier, P.; Martin, P. M.; Manara, D.; Dardenne, K.; Rothe, J.; Fossati, P. C. M.; Guéneau, C. Investigation of the Solid/Liquid Phase Transitions in the U−Pu−O System. *Calphad* **2023**, *80*, No. 102523.

(2) Kato, M.; Ikusawa, Y.; Sunaoshi, T.; Nelson, A. T.; McClellan, K. J. Thermal Expansion Measurement of (U,Pu)O_{2-x} in Oxygen Partial Pressure-Controlled Atmosphere. *J. Nucl. Mater.* **2016**, *469*, 223−227.

(3) Gibby, R. L.; Leibowitz, L.; Kerrisk, J. F.; Clifton, D. G. Analytical Expressions for Enthalpy and Heat Capacity for Uranium-Plutonium Oxide. *J. Nucl. Mater.* **1974**, *50* (2), 155−161.

(4) Prieur, D.; Vigier, J.-F.; Rothe, J.; Somers, J. Comparison of XRD, XANES and TGA Methods to Assess the O/M Ratio of $Th_{0.60}Am_{0.40}O_{2-x}$. *J. Nucl. Mater.* **2014**, *448* (1), 4−7.

(5) Epifano, E.; Naji, M.; Manara, D.; Scheinost, A. C.; Hennig, C.; Lechelle, J.; Konings, R. J. M.; Guéneau, C.; Prieur, D.; Vitova, T.; Dardenne, K.; Rothe, J.; Martin, P. M. Extreme Multi-Valence States in Mixed Actinide Oxides. *Commun. Chem.* **2019**, *2* (1), No. 59.

(6) Vigier, J.-F.; Martin, P. M.; Martel, L.; Prieur, D.; Scheinost, A. C.; Somers, J. Structural Investigation of $(U_{0.7}Pu_{0.3})O_{2-x}$ Mixed Oxides. *Inorg. Chem.* **2015**, *54* (11), 5358−5365.

(7) Martin, P.; Grandjean, S.; Valot, C.; Carlot, G.; Ripert, M.; Blanc, P.; Hennig, C. XAS Study of $(U_{1-y}Pu_y)O_2$ Solid Solutions. *J. Alloys Compd.* **2007**, *444−445*, 410−414.

(8) Bès, R.; Rivenet, M.; Solari, P.-L.; Kvashnina, K. O.; Scheinost, A. C.; Martin, P. M. Use of HERFD−XANES at the U L3- and M4-Edges To Determine the Uranium Valence State on $[Ni(H_2O)_4]_3[U(OH,H_2O)(UO_2)_8O_{12}(OH)_3]$. *Inorg. Chem.* **2016**, *55*, 4260.

(9) Kvashnina, K. O.; Kvashnin, Y. O.; Vegelius, J. R.; Bosak, A.; Martin, P. M.; Butorin, S. M. Sensitivity to Actinide Doping of Uranium Compounds by Resonant Inelastic X-Ray Scattering at Uranium L_3 Edge. *Anal. Chem.* **2015**, *87* (17), 8772−8780.

(10) Prieur, D.; Carvajal-Nunez, U.; Vitova, T.; Somers, J. Local and Electronic Structure of Americium-Bearing PuO_2. *Eur. J. Inorg. Chem.* **2013**, *2013* (9), 1518−1524.

(11) Noyau, S.; Audubert, F.; Martin, P. M.; Maitre, A. Influence of the Oxygen Potential on the Sintering of UO_2−45% PuO_2. *J. Eur. Ceram. Soc.* **2015**, *35* (13), 3651−3663.

(12) Vauchy, R.; Belin, R. C.; Robisson, A.-C.; Lebreton, F.; Aufore, L.; Scheinost, A. C.; Martin, P. M. Actinide Oxidation State and O/M Ratio in Hypostoichiometric Uranium−Plutonium−Americium $U_{0.750}Pu_{0.246}Am_{0.004}O_{2-x}$ Mixed Oxides. *Inorg. Chem.* **2016**, *55* (5), 2123−2132.

(13) Prieur, D.; Martin, P. M.; Jankowiak, A.; Gavilan, E.; Scheinost, A. C.; Herlet, N.; Dehaudt, P.; Blanchart, P. Local Structure and Charge Distribution in Mixed Uranium−Americium Oxides: Effects of Oxygen Potential and Am Content. *Inorg. Chem.* **2011**, *50* (24), 12437−12445.

(14) Lebreton, F.; Martin, P. M.; Horlait, D.; Bès, R.; Scheinost, A. C.; Rossberg, A.; Delahaye, T.; Blanchart, P. New Insight into Self-Irradiation Effects on Local and Long-Range Structure of Uranium−Americium Mixed Oxides (through XAS and XRD). *Inorg. Chem.* **2014**, *53* (18), 9531−9540.

(15) Belin, R. C.; Martin, P. M.; Léchelle, J.; Reynaud, M.; Scheinost, A. C. Role of Cation Interactions in the Reduction Process in Plutonium−Americium Mixed Oxides. *Inorg. Chem.* **2013**, *52* (6), 2966−2972.

(16) Osaka, M.; Kurosaki, K.; Yamanaka, S. Chemical Thermodynamic Analysis of Americium-Containing UO_2 and $(U,Pu)O_2$. *J. Alloys Compd.* **2007**, *428* (1−2), 355−361.

(17) Vauchy, R.; Robisson, A.-C.; Martin, P. M.; Belin, R. C.; Aufore, L.; Scheinost, A. C.; Hodaj, F. Impact of the Cation Distribution Homogeneity on the Americium Oxidation State in the $U_{0.54}Pu_{0.45}Am_{0.01}O_{2-x}$ Mixed Oxide. *J. Nucl. Mater.* **2015**, *456*, 115−119.

(18) Osaka, M.; Namekawa, T.; Kurosaki, K.; Yamanaka, S. Chemical Thermodynamic Representation of $(U,Pu,Am)O_{2-x}$. *J. Nucl. Mater.* **2005**, *344* (1−3), 230−234.

(19) Kato, M.; Konashi, K. Lattice Parameters of (U,Pu,Am,Np)-O_{2-x}. *J. Nucl. Mater.* **2009**, *385* (1), 117−121.

(20) Nakamichi, S.; Kato, M.; Tamura, T. Influences of Am and Np on Oxygen Potentials of MOX Fuels. *Calphad* **2011**, *35* (4), 648−651.

(21) Quemet, A.; Ruas, A.; Esbelin, E.; Dalier, V.; Rivier, C. Development and Comparison of Two High Accuracy Methods for Uranium Concentration in Nuclear Fuel: ID-TIMS and K-Edge Densitometry. *J. Radioanal. Nucl. Chem.* **2019**, *321* (3), 997−1004.

(22) Somers, J.; Glatz, J.-P.; Haas, D.; Wegen, D. H.; Fourcaudot, S.; Fuchs, C.; Stalios, A.; Plancq, D.; Mühling, G. *Status of the TRABANT Irradiation Experiments*. In Global'99: International Conference on Future Nuclear Systems-Nuclear Technology-Bridging the Millennia, Las Vegas, NV (United States); 1999.

(23) Vauchy, R.; Fouquet-Metivier, P.; Martin, P. M.; Maillard, C.; Solinhac, I.; Guéneau, C.; Léorier, C. New Sample Stage for Characterizing Radioactive Materials by X-Ray Powder Diffraction: Application on Five Actinide Dioxides ThO_2, UO_2, NpO_2, PuO_2 and AmO_2. *J. Appl. Crystallogr.* **2021**, *54*, 636−643, DOI: 10.1107/S1600576721002235.

(24) Rietveld, H. M. A Profile Refinement Method for Nuclear and Magnetic Structures. *J. Appl. Crystallogr.* **1969**, *2* (2), 65−71.

(25) TOPAS V4. *General Profile and Structure Analysis Software for Powder Diffraction Data, User's Manual*; Bruker AXS: Karlsruhe, Germany, 2008.

(26) Thompson, P.; Cox, D. E.; Hastings, J. B. Rietveld Refinement of Debye−Scherrer Synchrotron X-Ray Data from Al2O3. *J. Appl. Crystallogr.* **1987**, *20* (2), 79−83.

(27) LLorens, I.; Solari, P. L.; Sitaud, B.; Bes, R.; Cammelli, S.; Hermange, H.; Othmane, G.; Safi, S.; Moisy, P.; Wahu, S.; Bresson, C.; Schlegel, M. L.; Menut, D.; Bechade, J.-L.; Martin, P.; Hazemann, J.-L.; Proux, O.; Auwer, C. D. X-Ray Absorption Spectroscopy Investigations on Radioactive Matter Using MARS Beamline at SOLEIL Synchrotron. *Radiochim. Acta* **2014**, *102* (11), 957−972.

(28) Zimina, A.; Dardenne, K.; Denecke, M. A.; Doronkin, D. E.; Huttel, E.; Lichtenberg, H.; Mangold, S.; Pruessmann, T.; Rothe, J.; Spangenberg, Th.; Steininger, R.; Vitova, T.; Geckeis, H.; Grunwaldt, J.-D. CAT-ACT—A New Highly Versatile x-Ray Spectroscopy Beamline for Catalysis and Radionuclide Science at the KIT Synchrotron Light Facility ANKA. *Rev. Sci. Instrum.* **2017**, *88* (11), No. 113113.

(29) Popa, K.; Raison, P. E.; Martel, L.; Martin, P. M.; Prieur, D.; Solari, P. L.; Bouëxière, D.; Konings, R. J. M.; Somers, J. Structural Investigations of PuIII Phosphate by X-Ray Diffraction, MAS-NMR and XANES Spectroscopy. *J. Solid State Chem.* **2015**, *230*, 169−174.

(30) Prieur, D.; Lebreton, F.; Martin, P. M.; Caisso, M.; Butzbach, R.; Somers, J.; Delahaye, T. Comparative XRPD and XAS Study of the Impact of the Synthesis Process on the Electronic and Structural Environments of Uranium−Americium Mixed Oxides. *J. Solid State Chem.* **2015**, *230*, 8−13.

(31) Ravel, B.; Newville, M. ATHENA, ARTEMIS, HEPHAESTUS: Data Analysis for X-Ray Absorption Spectroscopy Using IFEFFIT. *J. Synchrotron Radiat.* **2005**, *12* (4), 537−541.

(32) Kvashnina, K. O.; Butorin, S. M.; Martin, P.; Glatzel, P. Chemical State of Complex Uranium Oxides. *Phys. Rev. Lett.* **2013**, *111* (25), No. 253002.

(33) Bès, R.; Kvashnina, K.; Rossberg, A.; Dottavio, G.; Desgranges, L.; Pontillon, Y.; Solari, P. L.; Butorin, S. M.; Martin, P. New Insight in the Uranium Valence State Determination in $U_yNd_{1-y}O_{2\pm x}$. *J. Nucl. Mater.* **2018**, *507*, 145−150.

(34) Talip, Z.; Wiss, T.; Di Marcello, V.; Janssen, A.; Colle, J.-Y.; Van Uffelen, P.; Raison, P.; Konings, R. J. M. Thermal Diffusion of Helium in ^{238}Pu-Doped UO_2. *J. Nucl. Mater.* **2014**, *445* (1−3), 117−127.

(35) Kato, M.; Komeno, A.; Uno, H.; Sugata, H.; Nakae, N.; Konashi, K.; Kashimura, M. Self-Radiation Damage in Plutonium and Uranium Mixed Dioxide. *J. Nucl. Mater.* **2009**, *393* (1), 134−140.

(36) Duriez, C.; Alessandri, J.-P.; Gervais, T.; Philipponneau, Y. Thermal Conductivity of Hypostoichiometric Low Pu Content $(U,Pu)O_{2-x}$ Mixed Oxide. *J. Nucl. Mater.* **2000**, *277* (2−3), 143−158.

(37) Prieur, D.; Martin, P.; Lebreton, F.; Delahaye, T.; Banerjee, D.; Scheinost, A. C.; Jankowiak, A. Accommodation of Multivalent Cations in Fluorite-Type Solid Solutions: Case of Am-Bearing UO_2. *J. Nucl. Mater.* **2013**, *434* (1−3), 7−16.

(38) Casalta, S.; Matzke, H. J.; Prunier, C. *A Thermodynamic Properties Study of the Americium-Oxygen System*. In Global 1995; ANS, 1995; vol. 2032, pp. 1667−1674.

(39) Saunders, N.; Miodownik, A. P. CALPHAD (Calculation of Phase Diagrams): A Comprehensive Guide. Vol. 1, 1st edition. https://www.elsevier.com/books/calphad-calculation-of-phase-diagrams-a-comprehensive-guide/saunders/978-0-08-042129-2.

(40) Computational Materials Engineering. Thermo-Calc Software. https://thermocalc.com/.

(41) Kurata, M. Thermodynamic Assessment of the Pu-U, Pu-Zr, and Pu-U-Zr Systems. *Calphad* **1999**, *23* (3), 305−337.

(42) Guéneau, C.; Dupin, N.; Sundman, B.; Martial, C.; Dumas, J.-C.; Gossé, S.; Chatain, S.; Bruycker, F. D.; Manara, D.; Konings, R. J. M. Thermodynamic Modelling of Advanced Oxide and Carbide Nuclear Fuels: Description of the U−Pu−O−C Systems. *J. Nucl. Mater.* **2011**, *419* (1−3), 145−167.

(43) Epifano, E.; Guéneau, C.; Belin, R. C.; Vauchy, R.; Lebreton, F.; Richaud, J.-C.; Joly, A.; Valot, C.; Martin, P. M. Insight into the Am−O Phase Equilibria: A Thermodynamic Study Coupling High-Temperature XRD and CALPHAD Modeling. *Inorg. Chem.* **2017**, *56* (13), 7416−7432.

(44) Epifano, E. Study of the U-Am-O Ternary Phase Diagram; Université Paris Saclay: Paris, 2017.

(45) Epifano, E.; Prieur, D.; Martin, P. M.; Guéneau, C.; Dardenne, K.; Rothe, J.; Vitova, T.; Dieste, O.; Wiss, T.; Konings, R. J. M.; Manara, D. Melting Behaviour of Uranium-Americium Mixed Oxides under Different Atmospheres. *J. Chem. Thermodyn.* **2020**, *140*, No. 105896.

(46) Fouquet-Métivier, P. *Study of the Influence of Americium on Thermodynamic and Structural Properties of* $(U,Pu)O_{2\pm x}$ *Mixed Oxides*; Université Paris Saclay, 2022. http://www.theses.fr/2017SACLX084.

(47) Vauchy, R.; Hirooka, S.; Watanabe, M.; Kato, M. Breaking the Hard-Sphere Model with Fluorite and Antifluorite Solid Solutions. *Sci. Rep.* **2023**, *13* (1), No. 2217.

(48) Guéneau, C.; Baichi, M.; Labroche, D.; Chatillon, C.; Sundman, B. Thermodynamic Assessment of the Uranium−Oxygen System. *J. Nucl. Mater.* **2002**, *304* (2−3), 161−175.

(49) Guéneau, C.; Chartier, A.; Fossati, P.; Van Brutzel, L.; Martin, P. 7.03 - Thermodynamic and Thermophysical Properties of the Actinide Oxides☆. In *Comprehensive Nuclear Materials*, 2nd ed.; Konings, R. J. M.; Stoller, R. E., Eds.; Elsevier: Oxford, 2020; pp 111−154.

(50) Wiss, T.; Dieste-Blanco, O.; Tacu, A.; Janssen, A.; Talip, Z.; Colle, J.-Y.; Martin, P.; Konings, R. TEM Study of Alpha-Damaged Plutonium and Americium Dioxides. *J. Mater. Res.* **2015**, *30* (9), 1544−1554.

(51) Kahraman, O.; Lebreton, F.; Martin, P.; Mermoux, M. Observable Consequences of Self-Irradiation Damage in a MIMAS-Type MOX Nuclear Fuel as Analyzed by x-Ray Diffraction, Electron Microprobe Analysis, and Raman Imaging. A Possible Methodological Approach. *J. Appl. Phys.* **2022**, *132* (11), No. 115106.